Angewandte Chemie
Eine Zeitschrift der Gesellschaft Deutscher Chemiker

Supporting Information

Loading-Dependent Structural Model of Polymeric Micelles Encapsulating Curcumin by Solid-State NMR Spectroscopy**

Ann-Christin Pöppler, Michael M. Lübtow, Jonas Schlauersbach, Johannes Wiest, Lorenz Meinel, and Robert Luxenhofer*

anie_201908914_sm_miscellaneous_information.pdf

Supporting Information

Content:

S1. Preparation of the CUR-Polymer Formulations and amorphous CUR

Curcumin (CUR) powder from *Curcuma longa* (Tumeric) was purchased from *Sigma-Aldrich* and used as received. The polymer, poly(2-methyl-2-oxazoline)-*block*-poly(2-n-propyl-2-oxazine)-*block*-poly(2-methyl-2-oxazoline) (PMeOx-*b*-PPrOzi-*b*-PMeOx ≡ A-pPrOzi-A ≡ **P**), was synthesized via living cationic ring-opening polymerization and characterized as described in detail in the literature.[1] This amphiphilic block-co-polymer forms micelles in the presence of guests in aqueous solution. The formulations with CUR were prepared using the thin film method as described in the same and previous work of this group.[1-2] Three different formulations with defined CUR loadings were prepared (**Table S1**).

Table S1: *Summary of the formulations used in this work and how they are referred to in the manuscript. The polymer A-pPrOzi-A was used to encapsulate Curcumin in its more hydrophobic core resulting in polymer micelles with a defined loading.*

Amount of loaded CUR per 10 g/L polymer	Name of Formulation	Loading in wt%
2 g/L	CUR-2-P	16.7
6 g/L	CUR-6-P	37.5
11 g/L	CUR-11-P	52.5

For the highest loading presented in this table, almost 25 molecules of CUR were incorporated, which is more than there are repeating units in the more hydrophobic inner polymer block.

Amorphous curcumin was obtained by quench cooling of the melted state with liquid N_2. A temperature of 200 °C, slightly above the 185 °C stated in the literature[3] were used and PXRD data was measured to confirm the amorphicity of the sample.

S2. Dissolution tests

Dissolution rates were measured with a Sirius T3 instrument (Sirius Analytical, Forest Row, UK) as described earlier.[4] Tablets discs (diameter 0.07 cm^2 and provided by the manufacturer of the machine) with defined surfaces were prepared by compression of 3–10 mg of each sample under a weight of 0.18 tons for 5 min with a manual hydraulic tablet press (Paul Weber, Stuttgart, Germany). The release of drug substance from the tablet discs allows data collection with a standardized surface area (0.07 cm^2) required to calculate dissolution rates.[4] Dissolution rates were determined photometrically at room temperature in simulated intestinal fluid (SIF) pH 6.8 (USP 26), for which the ionic strength was adjusted to 0.15 M with potassium chloride, at a stirring speed of 4800 rpm following manufacturer's instructions. The amount of dissolved CUR was calculated by the Beer-Lambert law using the spectroscopic data obtained by a fibre optic dip probe connected to a diode array detector. The linear part of the release profile was used for calculation of the dissolution rate (dissolved substance per time and surface area). In total, five samples were measured: crystalline and amorphous curcumin as well as three formulations. Each experiment was repeated three times. A two-sided t-test with a significance level of $p \leq 0.05$ was successfully performed for CUR-2-P and CUR-6-P as well as for CUR-11-P and amorphous CUR.

S2.1 pK_a determination of Curcumin

A photometrical pK_a assay as described[5] is necessary before performing the dissolution tests. The curcumin concentration was calculated with the mean molar extinction coefficients of the differently charged curcumin species derived from this assay. The three distinct pK_a values of 8.03 (± 0.14), 8.16 (± 0.03) and 10.16 (± 0.04) (**Figure S1**) were determined.[6] As the used buffer in the dissolution assay has a pH of 6.8, the predominant curcumin species in solution is H_3A (uncharged).

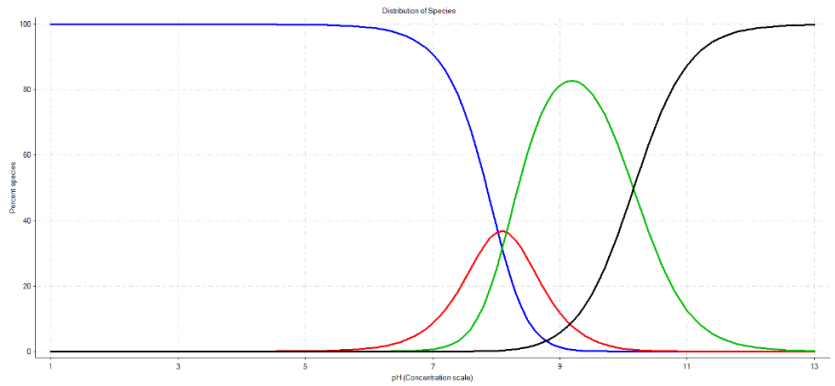

***Figure S1**: pH dependent distribution of Curcumin species. Blue H_3A (uncharged), red H_2A^-, green HA^{2-} and black A^{3-}*

S6.2 Pure as-received and amorphous Curcumin

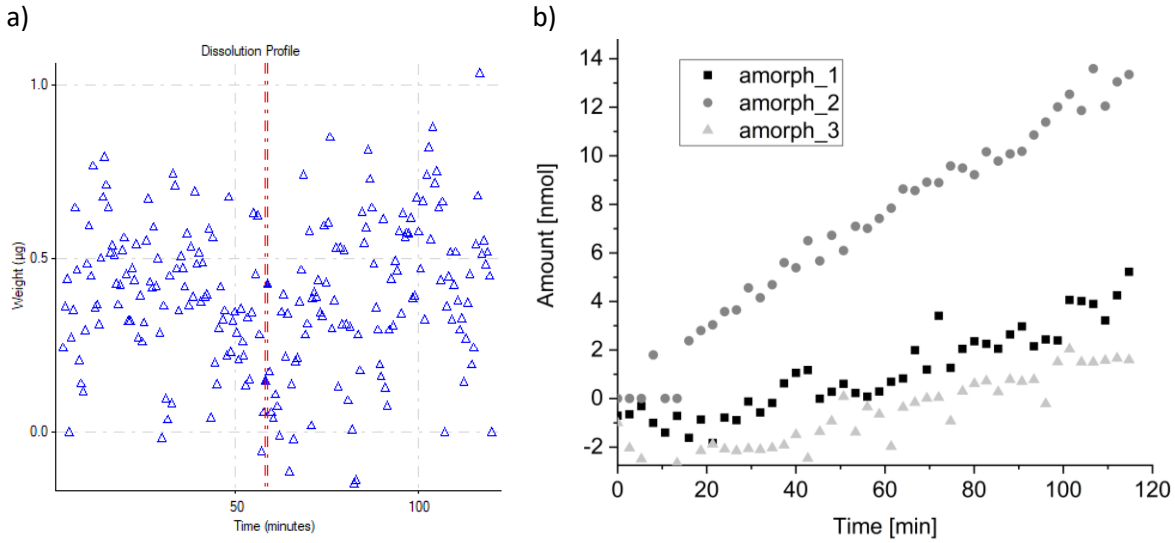

***Figure S2**: Exemplary dissolution profile for a) as-received and b) amorphous curcumin according to the protocol described above. For crystalline curcumin no dissolution could be detected within the duration of the experiment, because the concentration was below the limit of detection (only signal noise).*

For as-received curcumin, the concentration was below the limit of detection (**Figure S2a**), which prevented the determination of the dissolution rate.

In the case of amorphous curcumin (obtained via quench-cooling), a higher dissolution rate could be expected. Exemplarily for the three repetition experiments, this is observed in **Figure S2b**. From the three experiments, an average extrapolated dissolution rate of 1.01 nmol/min*cm² can be determined. The individual values 0.78, 1.51 and 0.75 nmol/min*cm² show that the deviation is quite

large. Residual small particles on the tablet disc can already interfere with the measurements for samples with such low amounts of detectable substance.

S2.3 Formulations CUR-2/6/11-P

For the three formulations, dissolution profiles with varying onset could be recorded for all samples (**Figure S3**).

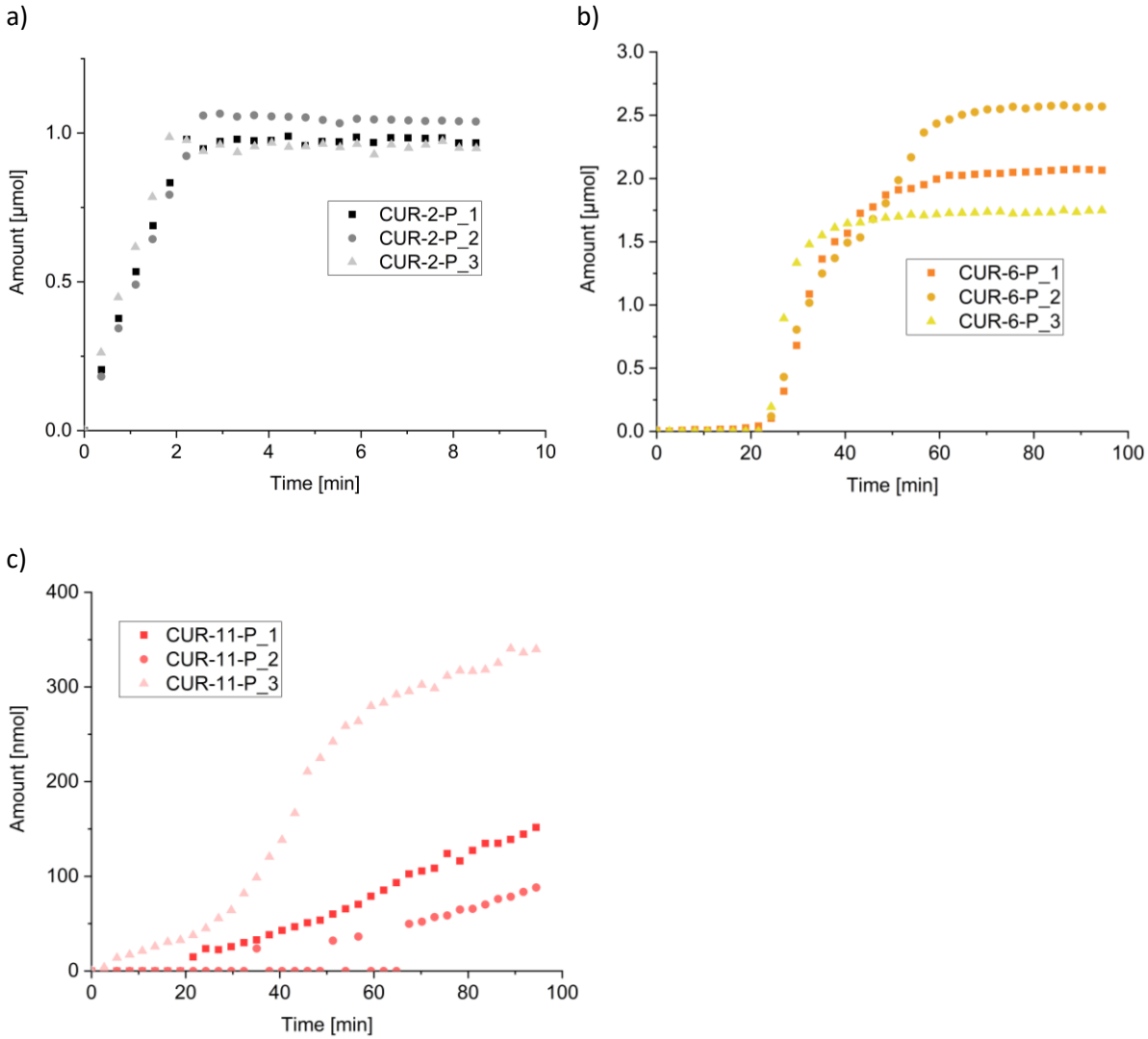

Figure S3: *Dissolution profiles for the three samples a) CUR-2-P, b) CUR-6-P and c) CUR-11-P recorded for a pressed tablet at pH 6.8 (n =3). While the y-axis is displayed in µmol for a) and b), the axis for CUR-11-P in c) is given in nmol.*

S3. Hygroscopicity

Storage of part of the sample under ambient conditions already indicated that the three formulations show different degrees of hygroscopicity. Therefore, the hygroscopicity of the three formulations was measured gravimetrically as explained in the European Pharmacopoeia (Ph. Eur.): The samples inside a glass vial are placed in a closed desiccator containing a saturated solution of ammonium chloride. Thus, a fixed relative humidity of 80% at 25°C is achieved.[7] After 24 h, the samples were removed from the desiccator and carefully weighed. From this, the weight gain [%] was determine for each sample. The data is summarized in **Table S2**. Comparably small sample volumes were used. However, a general trend is distinguishable, and the difference observed between CUR-2-P and CUR-6-P is very pronounced, which agrees with dissolution data. Furthermore, the pMeOx polymer block starting to be involved in the CUR coordination for CUR-6-P and the CUR molecules thus being located closer to the particle's surface should result in an increase in surface hygroscopicity.

***Table S2**: Experimental results from the hygroscopicity test according to the European Pharmacopoeia (Ph. Eur.). Weighing of the vials was carried out with a high-precision balance. The temperature was 24 °C and thus slightly lower than the temperature given in the Ph. Eur. A saturated solution of ammonium chloride was used to generate the 80% RH atmosphere in the desiccator.*

	empty glass [mg]	**filled glass [mg]**	**after 24h [mg]**	**Sample [mg]**	**Hygroscopicity [%]**
CUR-2-P	7675.3	7682.9	7685.2	7.6	**30**
CUR-6-P	7685.7	7694.5	7695.9	8.8	**16**
CUR-11-P	7710.7	7719.6	7720.9	8.9	**15**

S4. Characterization of the Formulations by NMR Spectroscopy in solution

All NMR experiments were performed on a 14.1 T standard bore Bruker Avance III instrument at room temperature. A 5 mm BBFO probe equipped with z-gradient and a temperature unit was used.

NMR spectroscopy in solution using $CDCl_3$ (readily dissolves polymer and CUR) was used for a first assignment of the ^1H and ^{13}C chemical shifts for the different components.

In the case of as received curcumin dissolved in $CDCl_3$, we saw the presence of the enol form only as previously shown.[8] The purity of the as-received curcumin was assessed using ^1H NMR spectra in $CDCl_3$. From the relative integral ratios of the central CH moiety of the three main components (**Figure S4**), curcumin, demethoxycurcumin (DMC) and bisdemethoxycurcumin (BDMC), the following composition could be determined: 77 % CUR : 18 % DMC : 5 % BDMC.

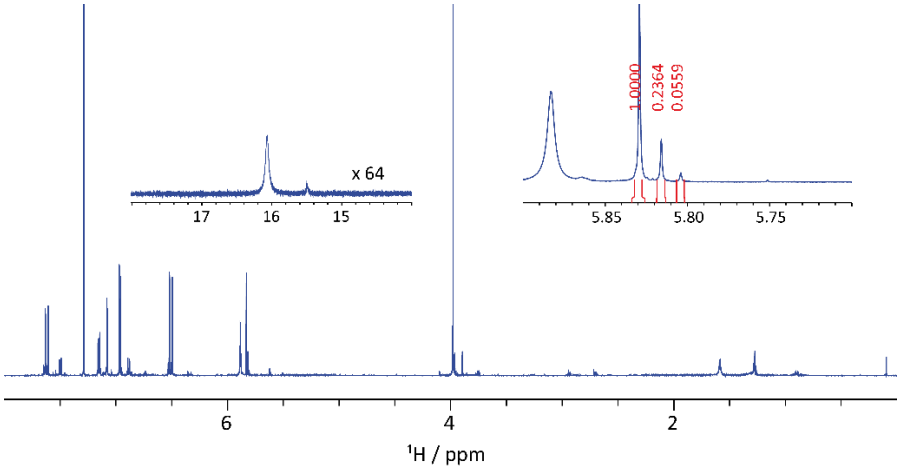

***Figure S4**: ^1H NMR spectrum of as-received CUR in $CDCl_3$. As there are no signals between 8 and 15 ppm, the enol resonance is shown as an insert. For the relative ratios of the three main components, the integrals for the central CH moiety were used.*

The ^1H as well as ^{13}C NMR spectra of the pure polymer in solution (no micelles) including assignment of the chemical shifts to the respective fragments in the polymer is shown in **Figure S5**. For the assignment a standard set of 1D and 2D NMR data (^1H, ^{13}C, ^1H-^1H COSY, ^1H-^{13}C HSQC, ^1H-^{13}C HMBC, ^1H-^1H NOESY) was used.

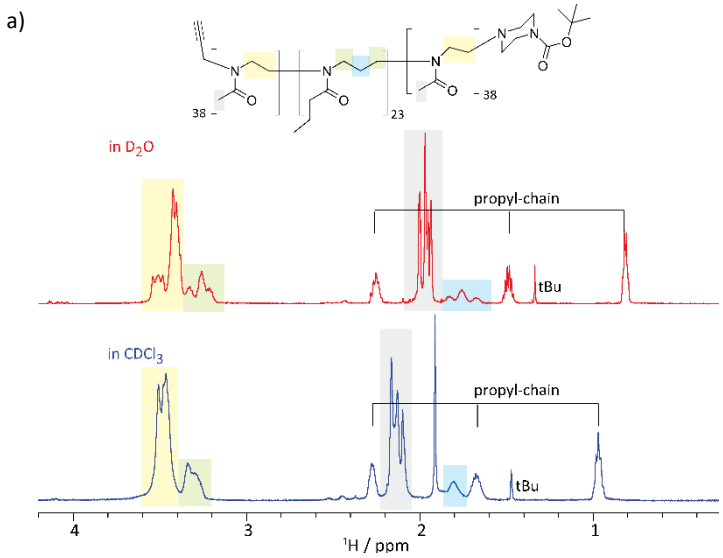

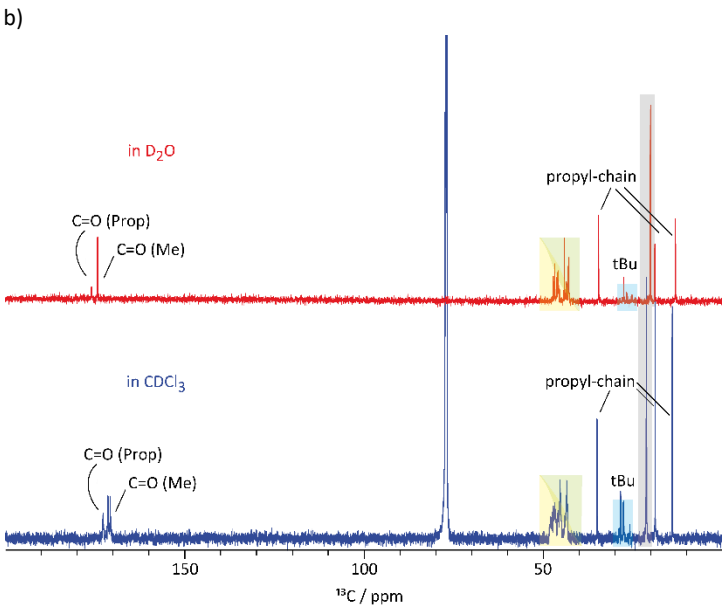

Figure S5: *a) ^{1}H and b) ^{13}C NMR spectra of the neat polymer in $CDCl_3$ (blue) and D_2O (red) recorded on a 600 MHz spectrometer. The chemical formula is shown on top of the proton data and assignment of the resonances is indicated by either colour or text fragments.*

Variably temperature NMR of CUR-2-P in D_2O solution was recorded:

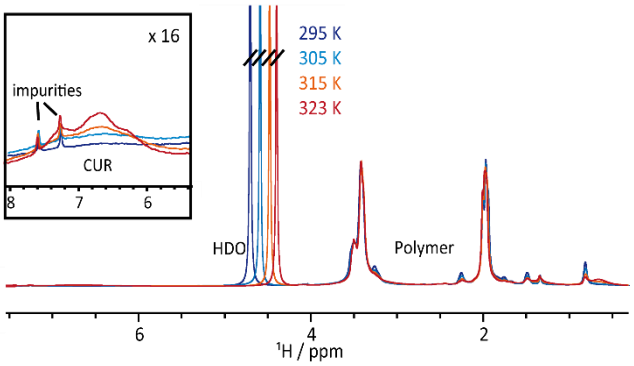

Figure S6: *Variable temperature ^{1}H NMR spectra of CUR-2-P in D_2O at 14.1 T.*

Increasing the mobility of the overall system by increasing the temperature resulted in narrower linewidths for the CUR signals, but they remained very broad features (**Figure S6**, inset).

DOSY

DOSY NMR data were measured at 298 K with a Bruker Avance III HD 600 MHz spectrometer and a 5 mm BBFO probe containing a z-axis gradient coil with a maximum gradient strength of 50 G cm^{-1}.To avoid the influence of convection effects on the results (due to temperature gradients in the coil of the probe), two different pulse sequences, a stimulated echo BPP-LED pulse sequence[9] with sample rotation and a corresponding double stimulated echo pulse sequence[10] without sample rotation were used. No differences in diffusion data obtained from the two pulse sequences were observed. For all experiments, the diffusion gradients were linearly incremented in 16 steps from 2 to 98%. Diffusion times Δ of 100 ms and durations of a bipolar gradient pulse δ of 4 ms were optimized and then used for all further experiments. All signals had decayed to below 5% of the initial signal area. The diffusion coefficients were obtained by fitting the decay curves of the signal area versus the gradient strength

with two exponentials according to $I = I_{0A}e^{-D_A\gamma^2\delta^2g^2\Delta'} + I_{0B}e^{-D_B\gamma^2\delta^2g^2\Delta'}$ for species A and B as included in the Bruker software Topspin 3.5. As starting values for the fitting routine of the diffusion coefficient $8{\cdot}10^{-12}$ and $9{\cdot}10^{-11}$ m²/s were chosen. The decay curves with the respective fit can be found below (**Figure S7**). The reported diffusion coefficients were obtained from pseudo-2D measurements with the BPP-LED pulse sequence and converted to approximate radii by using the viscosity of D_2O at 298 K.[11] To extract the values shown in **Table S3**, the $CH_3(CO)$ resonance of the hydrophilic polymer block at 1.98 ppm was used as this functional group is located in the shell of the micelles and the signal is clearly separated.

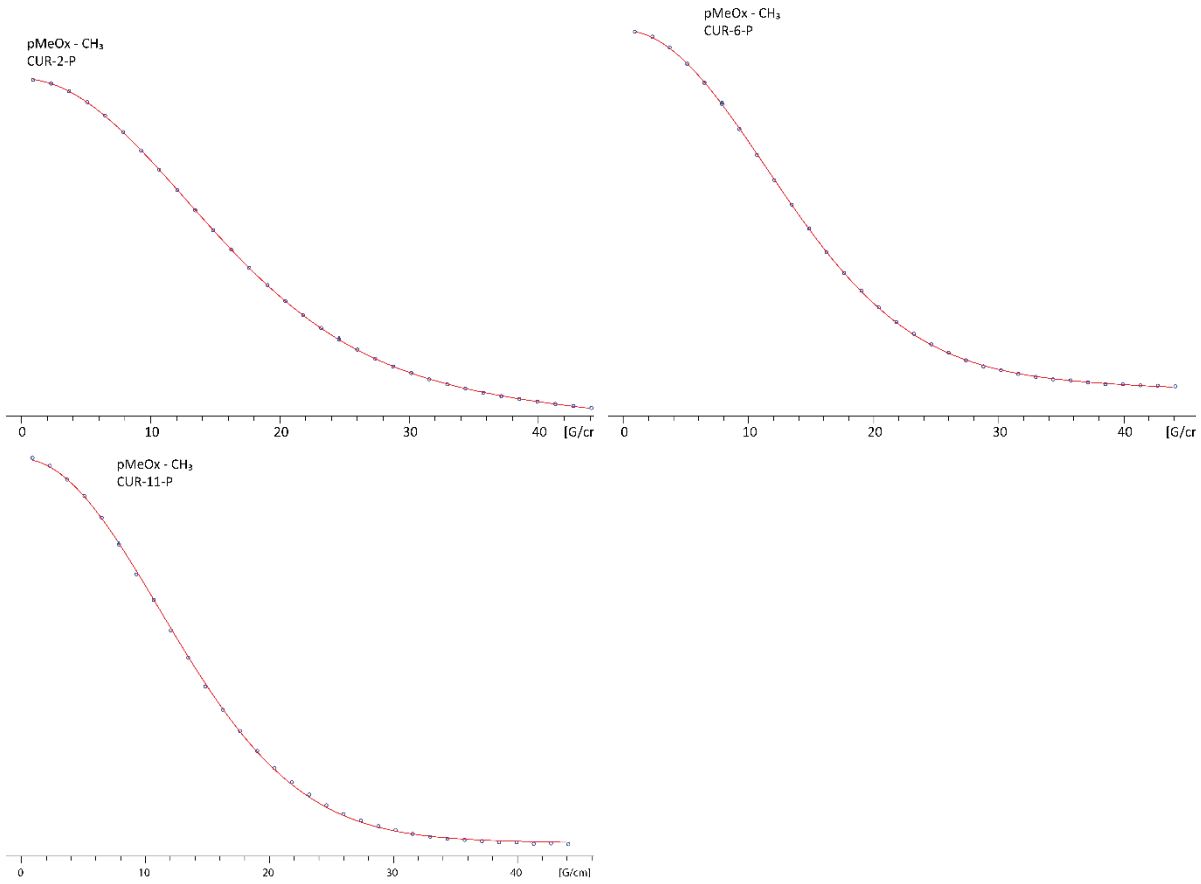

Figure S7: *Decay curves and corresponding biexponential fit for the CH_3 group of the pMeOx polymer block as obtained from the topspin fitting routine for the re-dispersed formulations CUR-2-P, CUR-6-P and CUR-11-P.*

Table S3*: Diffusion coefficients and approximated radii of the three formulations with increasing drug loading obtained from ^{1}H DOSY NMR data using two exponentials to fit the decay curves. The values shown were extracted for the $CH_3(CO)$ signal at 1.98 ppm. The radii are compared to diameters determined by dynamic light scattering (DLS) as found in literature.*

Formulation	Diffusion coefficients D [m²/s]	Radii approximated from D [nm]	Diameter by DLS [nm] and (drug loading)[1]	Diameter by DLS [nm] and (drug loading)[12]	Diameter by DLS [nm] and (drug loading)[13]
CUR-2-P (10/2)	$1.72{\cdot}10^{-11}$ $7.56{\cdot}10^{-11}$	11.5 2.6	22.9 (10/2)	20 (10/3)	29 (10/2)
CUR-6-P (10/6)	$1.62{\cdot}10^{-11}$ $8.95{\cdot}10^{-11}$	12.2 2.2	25.3 (10/5)	19 (10/5)	24 (10/6)
CUR-11-P (10/11)	$8.01{\cdot}10^{-12}$ $9.12{\cdot}10^{-11}$	24.8 2.2	46.5 (10/11)	48 (10/12)	52 (10/12)

For all samples, diffusion coefficients in a similar range were determined. One of the two components diffuses faster than the second species and thus has a smaller size. The size of this smaller particle was determined to be 2.2-2.6 nm and possibly results from unimers (single polymer strands) present in solution,[14] while the larger particles have varying radii depending on the CUR loading. At low and medium CUR loading, the radius of the micelles formed in solution is in a similar range (11.5 and 12.2), while a doubling in size is observed upon increasing the loading further (CUR-11-P). This agrees with the literature-known values observed by dynamic light scattering (DLS) shown in **Table S3**. The DLS data shown here is from three different publications in the last years, measured with two different setups and shows similar sizes for CUR-2-P and CUR-6-P, while a large increase is observed for the highest loading. Here, only the values closest to the formulations used in this work are shown, while the individual publications contain values for a larger number of differently loaded formulations.

S5. Characterization by solid-state NMR Spectroscopy

The solid-state NMR measurements were performed using a 3.2 mm double-channel Bruker probe at 14.1 T and 24 kHz MAS. For the CP, a 2 ms ramp (50 to 100%) on the ^{1}H channel was used during the CP contact time for all samples. For heteronuclear decoupling during acquisition, SPINAL64 was employed with a 100 kHz nutation frequency (^{1}H). The chemical shifts were referenced using adamantane (left signal at 38.48 ppm) by subsequent adjustment of the magnetic field.

For the characterization by both NMR spectroscopy and calculations, the following numbering scheme and assignment is used in accordance with previously published data on CUR (**Figure S8a**).[15]

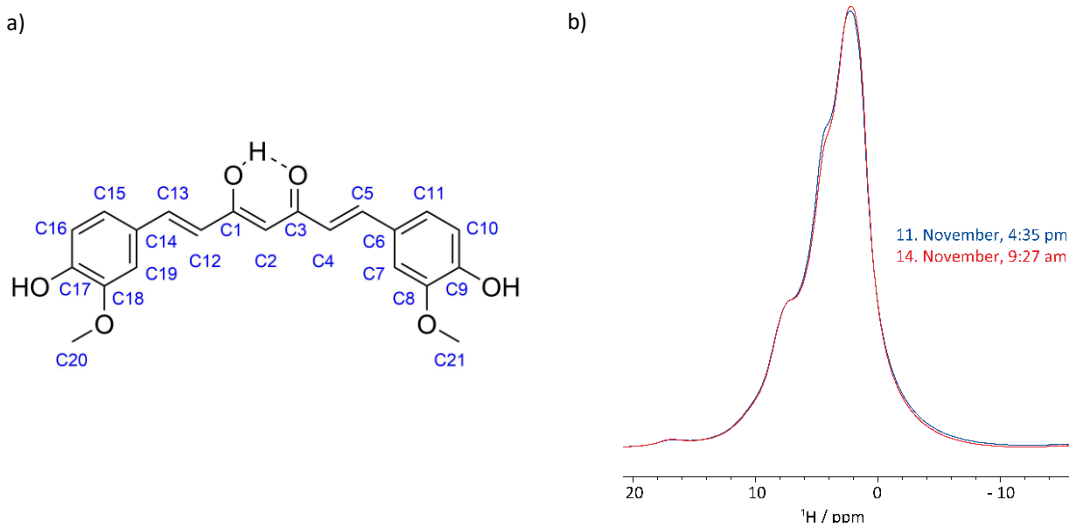

Figure S8: *a) Numbering scheme for the curcumin molecule as is used throughout this manuscript. H-atoms are labelled according to the carbon to which they are attached. b) ^{1}H solid-state NMR spectra of the formulation CUR-2-P recorded at the beginning of the measurement block and after spinning the sample at 24 kHz for ~2.5 days.*

In **Figure S8b**, the ^{1}H solid-state NMR spectra of the formulation CUR-2-P are shown. Both spectra were measured using the same conditions, yet at different times of the measurement block to ensure that the sample is unchanged by the forces caused by rotating the sample at 24 kHz. At this MAS rate, the signal overlap is substantial, which makes the interpretation of features and trends more difficult. Higher MAS rates would be necessary to make use of powerful proton-detected solid-state NMR experiments. Therefore, the focus in this manuscript is on the ^{13}C NMR spectroscopic data.

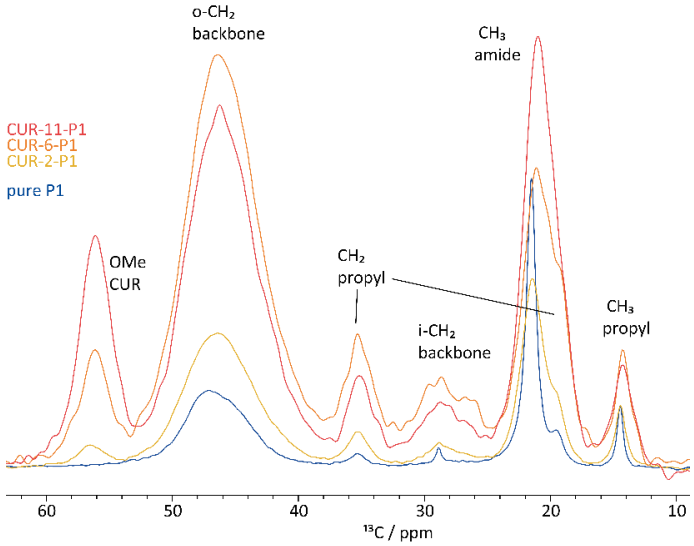

***Figure S9**: Extract from the ^{13}C CP/MAS NMR spectra of the formulations CUR-2/6/11-P as well as pure polymer for comparison. Only the signal areas of the aliphatic polymer signals and that of the OMe group of CUR are shown (the complete spectra are displayed in Figure 2 of the main manuscript). Scaling was applied according to the individual number of scans.*

To look at the changes in the polymer ^{13}C NMR signals in more detail, the respective area in the ^{13}C CP/MAS spectra of the pure polymer P (blue) as well as the three formulations is shown in **Figure S9**. The OMe signal of CUR indicates the increasing CUR loading of the micelles. The corresponding amount of polymer should be decreasing. Interestingly, an increase in the signal intensity is observed, which can result from the less mobile arrangement and/or a larger number of proton-carbon contacts. If we first focus on the CH_3 group of the propyl moiety (inner polymer block), we see a trend similar to the one observed for the amide group of the outer polymer blocks. The chemical shift decreases with increasing loading with CUR-6-P and CUR-11-P having very similar values, which is mirrored by the line widths (pure polymer: 96 Hz; CUR-2-P: 168 Hz; CUR-6-P: 269 Hz; CUR-11-P: 291 Hz). Again, the difference from pure polymer to the low and medium loadings are larger than the difference between medium and high loading, for which we propose that the core is already full and additional CUR needs to be located at the hydrophobic-hydrophilic interface with the amide groups of the hydrophilic blocks participating in the coordination. An indicator for the location of CUR at the interface could be the behaviour of the signal at 29 ppm, which belongs to the inner CH_2 group of the backbone. The signal broadens and for the two higher loadings, the signal consists of two separate parts (~28 and 29 ppm).

A table summarizing all chemical shifts and (if possible to determine) linewidths for amorphous CUR, the pure polymer and the three formulations CUR-2/6/11-P is shown in **Table S4**.

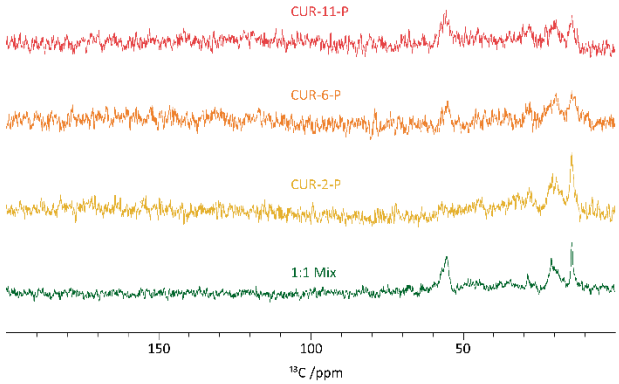

***Figure S10:** Direct excitation ^{13}C solid-state NMR spectra of CUR-2-P (yellow), CUR-6-P (orange), CUR-11-P (red) and a 1:1 physical mixture of CUR and the polymer (green). The spectra were measured using a short relaxation delay of 0.8 s and 256 scans at 14.1 T and 20 kHz MAS.*

Additional ^{13}C NMR spectra obtained by direct excitation with a short relaxation delay of 0.8 s revealed that for low loadings, the mobility of the pMeOx unit and propyl chain is still maintained, while this is reduced at higher loadings.

***Table S4**: Summary of the chemical shifts in ppm and line widths (if possible as full width at half maximum in Hz) determined from the ^{13}C CP/MAS NMR spectra of the three formulations CUR-2-P, CUR-6-P and CUR-11-P, which are compared to amorphous curcumin as well as the pure polymer. An increase compared to the pure compound is indicated in red, a decrease in blue.*

Cur		P1		Cur-2-P1				Cur-6-P1				Cur-11-P1			
ppm	FWHM (in Hz)	ppm	FWHM (in Hz)	ppm	ΔShift	FWHM	ΔFWHM	ppm	ΔShift	FWHM	ΔFWHM	ppm	ΔShift	FWHM	ΔFWHM
55.9	528.2			56.56	0.66	410.83	-117.3	56.17	0.27	480.15	-48.0	56.09	0.2	494.34	-33.8
103.4	xxx			102.99	-0.36	xxx	xxx	102.46	-0.9	657.29	xxx	102.80	-0.5	532.36	xxx
107.7	xxx			109.60	1.91	*635.50*	*xxx*	xxx	xxx	xxx	xxx	108.71	1.0	xxx	xxx
115.7	778.8			116.52	0.86	*506.98*	-271.8	116.95	1.29	671.28	-107.5	116.46	0.8	682.92	-95.9
120.9	xxx			121.64	0.71	xxx	xxx	121.00	0.07	xxx	xxx	121.19	0.3	xxx	xxx
127.7	623.0			127.61	-0.12	*506.97*	-116.1	127.49	-0.2	554.00	-69.0	127.63	-0.1	521.60	-101.4
141.8	940.6			141.47	-0.32	710.48	-230.1	141.56	-0.2	*819.92*	*-120.7*	141.17	-0.6	849.61	-91.0
147.9	552.1			149.47	1.62	485.55	-66.6	149.48	1.63	502.71	-49.4	148.92	1.1	489.33	-62.8
183.4	1890.3			184.22	0.85	1142.98	-747.4	184.11	0.74	1302.07	-588.3	184.11	0.7	1279.34	-611.0
		14.4	96.3	14.43	0.0	167.50	71.2	14.22	-0.2	269.07	172.8	14.22	-0.2	290.94	194.6
		19.5	212.58	*19.57*	0.03	*235.86*	*23.3*	*19.36*	-0.2	333.14	120.6	xxx	xxx	xxx	xxx
		21.5	140.39	21.40	-0.1	335.00	194.6	21.12	-0.4	461.26	320.9	21.03	-0.5	427.40	287.0
		28.8	126.35	28.79	-0.1	565.72	439.4	26.42	-2.4	xxx	xxx	28.62	-0.2	744.09	617.7
								29.19	0.35	615.02	488.67				
		35.3	288.49	35.26	-0.1	333.28	44.8	35.25	-0.1	486.89	198.4	35.13	-0.2	435.12	146.6
		47.1	903.440	46.35	-0.7	1013.52	110.1	46.39	-0.7	1075.80	172.4	46.21	-0.9	1040.17	136.7
	overlapping	*171.9*	*310.56*	a)		xxx	xxx	a)		xxx	xxx	a)		xxx	xxx

a) In the 1D datasets, which were used as basis for this table, the peak positions and line widths of the carbonyl resonance of the amide group are difficult to determine due to severe signal overlap. Please see Figure 4 in the main text for more information.

^{1}H-^{13}C FSLG HETCOR data using SPINAL64 heteronuclear decoupling (100kHz):

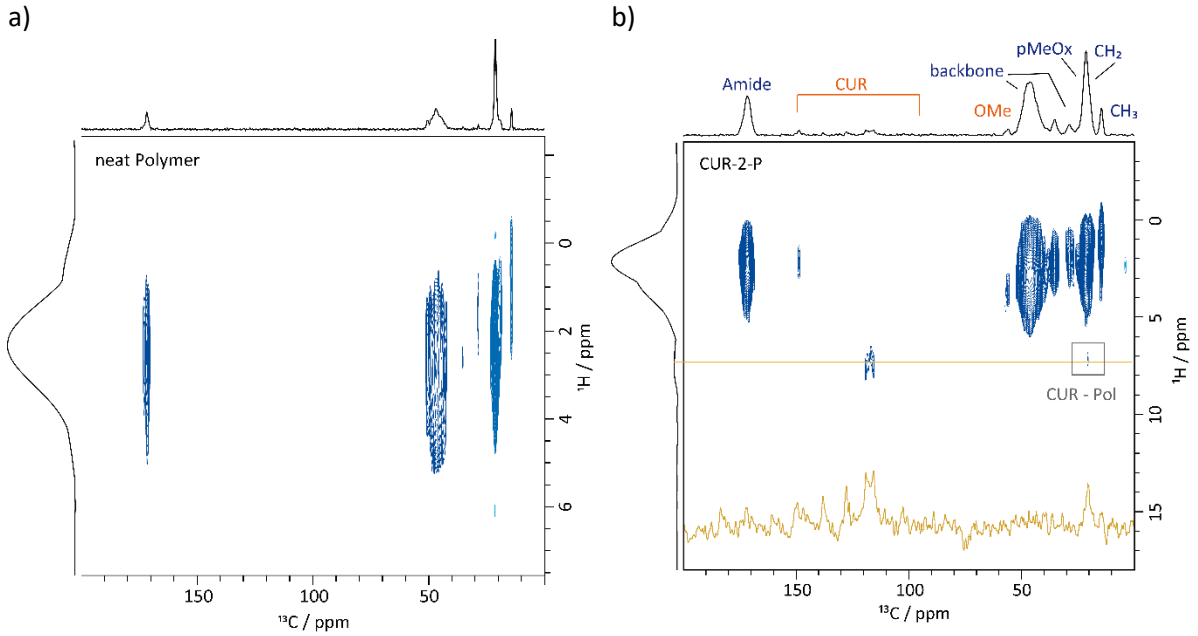

Figure S11: *^{1}H-^{13}C FSLG HETCOR spectra of a) the neat polymer with a contact time of 1.5 ms at 24 kHz MAS and b) CUR-6-P recorded with 5 ms of contact time at 20 kHz MAS. Both spectra were obtained at 14.1 T. For a) 136 transients were co-added for each of the 100t_1 FIDs, for b) 368 transients were co-added for each of the 64 t_1 FIDs. Additionally, to improve signal to noise, only the first 8.4 ms of the fast decaying FID were used.*

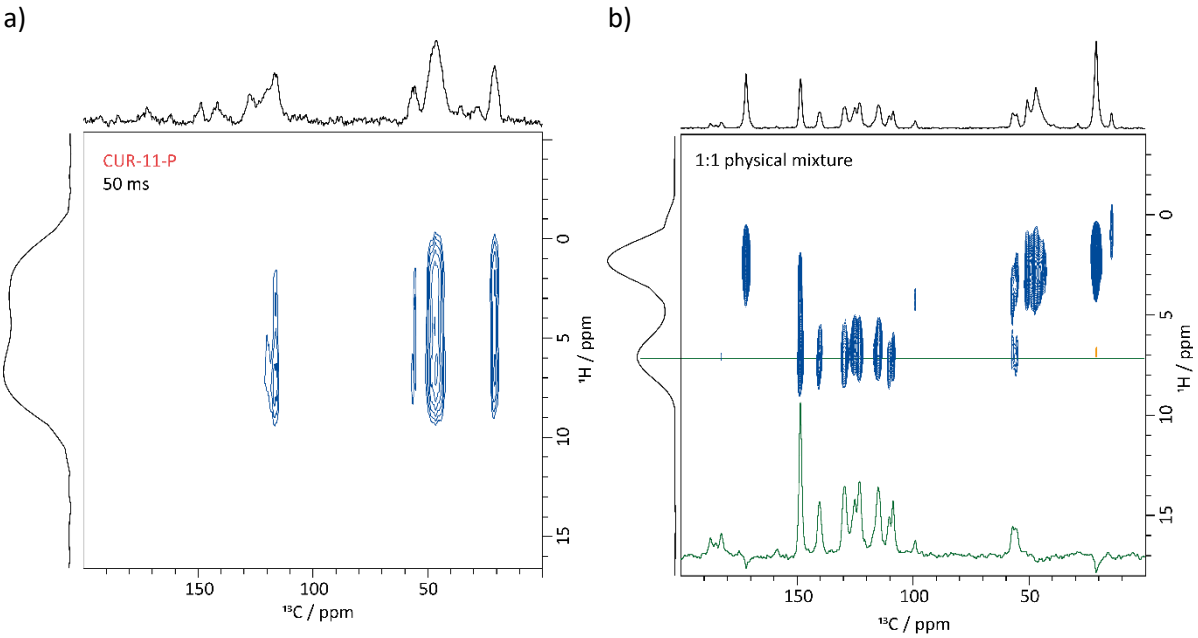

Figure S12: *a) ^{1}H-^{13}C FSLG HETCOR spectrum of CUR-11-P acquired with an additional spin-diffusion time of 50 ms and a contact time of 0.3 ms according to the work of Duan et al.[16] and b) ^{1}H-^{13}C FSLG HETCOR spectrum of a 1:1 physical mixture of CUR and the neat polymer recorded with 5 ms of contact time. Both spectra were obtained at 14.1 T and 20 kHz MAS. For a) 368 transients were co-added for each of the 50t_1 FIDs, for b) 256 transients were co-added for each of the 46 t_1 FIDs.*

S6. Characterization of the Formulations by Powder X-ray diffraction

Powder diffractometric studies were done with a Bruker Discover D8 powder diffractometer (Karlsruhe, Germany) using Cu Kα radiation (unsplit $K\alpha_1$+$K\alpha_2$ doublet, mean wavelength λ = 154.19 pm) at a power of 40 kV and 40 mA, a focusing Goebel mirror and a 2.5° axial Soller slit. The scattered X-ray beam went through a receiving slit (3,3°). Detection was done with a LynxEye-1D-Detector (Bruker AXS) using the full detector range of 192 channels. Measurements were done in reflection geometry in coupled two theta/theta mode with a step size of 0.025° in 2θ and 0.55 s (pure compounds) or 0.71 s (formulations) measurement time per step in the range of 5–50°(2θ). Data collection was done with the software package DIFFRAC.Suite (V2 2.2.690, BrukerAXS 2009–2011, Karlsruhe, Germany). The diffraction data was subsequently converted into ASCII format and further handled with Origin (OriginLab, Massachusetts, USA).

Directly after sample preparation, PXRD data was recorded confirming the amorphous nature of the freeze-dried formulations (**Figure S13**).

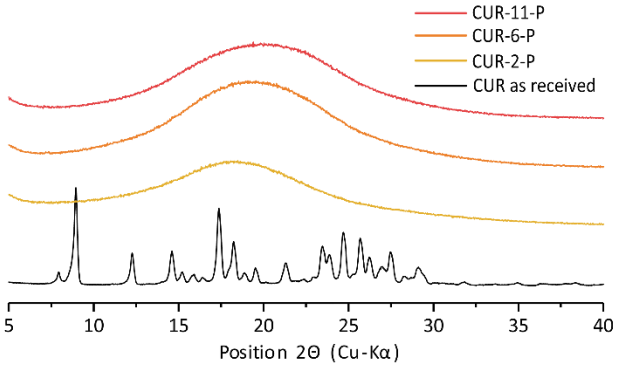

***Figure S13**: PXRD patterns recorded for as-received curcumin and the formulations, CUR-2-P, CUR-6-P and CUR-11-P.*

The typical amorphous halo is generally similar in all three formulations, but trends are observed, as the diffraction peaks become broader and shift to higher 2θ values from low (yellow) to high loading (red). As the PRXD patterns depend on sample composition and arrangement of the individual components,[17] this indicates changes in local order.

After the measurements undertaken (NMR spectroscopy, dissolution tests), PXRD data was recorded again to ensure that the samples did not change under the measurement conditions (e.g. Magic Angle Spinning (MAS)).

S6.1 Pure Curcumin and the Effect of MAS

Curcumin was first measured by PXRD as purchased and thus as it was used for the preparation of the formulations (**Figure S14a**). As expected for a microcrystalline compound, discrete peaks were detected (black), which agree well with simulated data from the literature known stable monoclinic form of CUR (BINMEQ05).[18] Additionally, the diffraction pattern for the quench-cooled, amorphous sample is shown in red. The sample is clearly X-ray amorphous and only very broad features centred around 16°, 24° and 43° (2*Θ*) can be observed. In a second step, diffractograms of the CUR-6-P formulation directly after preparation and after one day at 24 kHz MAS are exemplarily shown (**Figure S14b**). There are no pronounced differences between the two samples, which confirms that the forces acting on the sample under MAS do not alter the general arrangement of the CUR-polymer assembly.

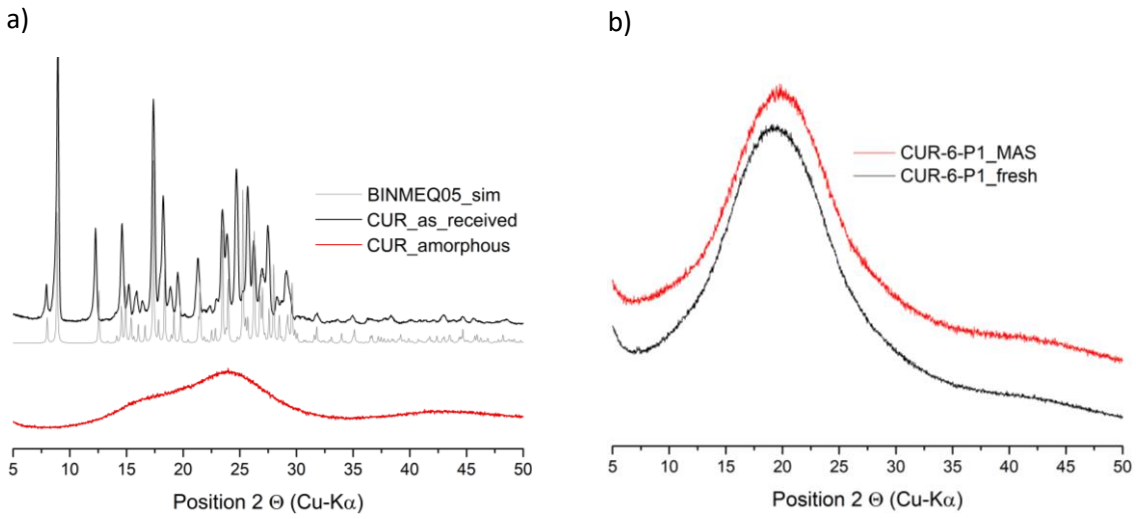

***Figure S14**: a) Powder X-ray pattern of as received curcumin with the corresponding simulated data from the monoclinic form BINMEQ05 alongside the data for the quench-cooled amorphous form. b) Comparison of the PXRD patterns before and after MAS at 24 kHz.*

S6.2 PXRD to ensure sample stability for dissolution testing

Similar to the examination before and after MAS, the pressing of the samples into the tablets prior to the dissolution tests exposes them to considerable pressure. Therefore, PXRD was recorded for the fresh samples and compared to the same samples after tablet pressing. The corresponding PXRD patterns for pure curcumin as well as for the CUR-6-P formulation are shown below (**Figure S15**).

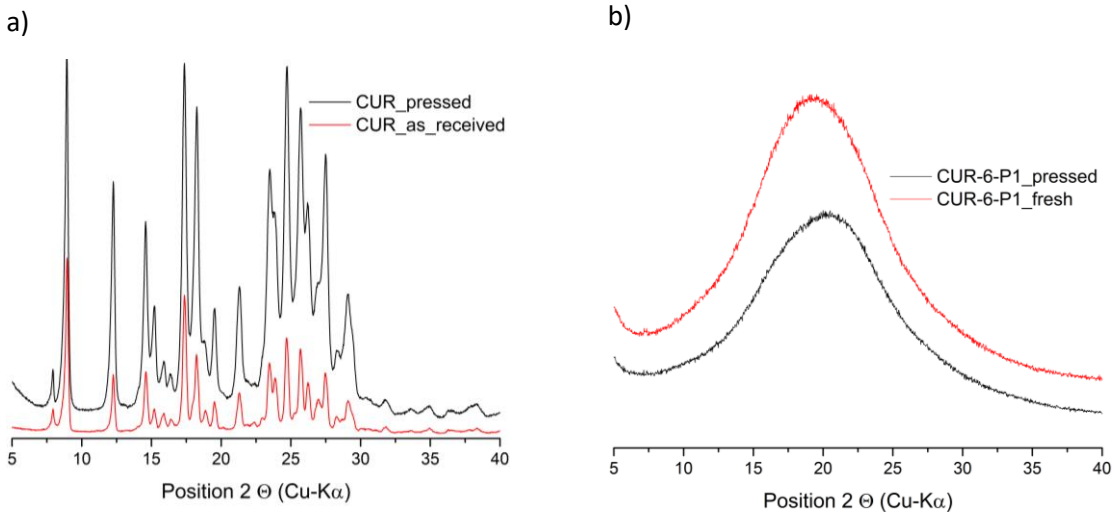

***Figure S15**: PXRD patterns for as-received curcumin (a) and the formulation CUR-6-P (b) before and after tablet pressing.*

In the case of as-received CUR (a), only changes in the peak intensities, but not in the peak positions are observed. This confirms that the cell and atom positions remain unchanged by the tablet pressing, but that preferred orientations of crystallites are influenced. For CUR-6-P representing the set of formulations (b), the general feature in the diffractogram is maintained.

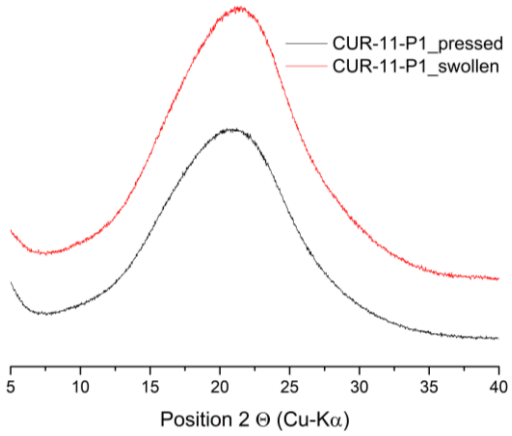

***Figure S16**: PXRD patterns of the pressed and subsequently swollen tablet of CUR-11-P.*

Finally, PXRD data was recorded for the swollen yet not dissolved tablet, which was observed for the highest CUR loading of the micelles. The data is compared to that of the pressed CUR-11-P tablet (**Figure S16**). The general appearance of the PXRD pattern does not change due to the dissolution experiment. Furthermore, no indication of crystalline, well-defined peaks is found within the detection limit of this experiment despite addition of three subsequent measurements for the swollen sample. This shows that the delay in the dissolution event is not likely to be due to crystallization processes at the interface.

S7. GIPAW(CASTEP) calculations of Curcumin

GIPAW (CASTEP) calculations[19] were used for: a) determination of dominant interactions in the crystalline materials, b) information on the influence of the geometry of the CUR molecules on the chemical shifts and c) additional calculations addressing the OH···O=CN interaction. In the following, a general information on the calculations will be given (**Chapters S7.1 and S7.2**) before specific data will be discussed (**Chapter S7.3, S7.4 and Chapter S8**).

S7.1 General Information on Version, Parameters and Conventions used

All calculations were run on the local cluster of the workgroup of Prof. Roland Mitric. They were performed using the CASTEP code,[19a] academic release version 17.2. All structures were first geometry optimized with the unit cell parameters fixed before chemical shieldings were calculated using the GIPAW method.[19b, 19c] In all calculations, the PBE exchange correlation was used.[20] For the plane wave basis set with ultra-soft pseudopotentials,[21] a maximum cut-off energy of 800 eV was used alongside a Monkhorst–Pack grid for sampling over the Brillouin zone with minimum sample spacing 0.1 × 2π $Å^{-1}$. The forces, energies and displacements were converged to better than 0.05 eV $Å^{-1}$, 0.00002 eV, and 0.001 Å, respectively. To handle and visualize NMR spectral output the Magresview environment was employed.[22] For a crystal *vs.* molecule comparison, an additional NMR calculation was performed for a single molecule from the optimized structure in an enlarged unit cell, which is thus no longer interacting with neighbouring molecules.

In this work, the chemical shielding tensors obtained by GIPAW (CASTEP) calculations are presented according to the *Haeberlen-Mehring-Spiess* convention:

The principal components of the chemical shielding tensor are σ_{xx}, σ_{yy} and σ_{zz}, satisfying $|\sigma_{zz} - \sigma_{iso}| \geq |\sigma_{xx} - \sigma_{iso}| \geq |\sigma_{yy} - \sigma_{iso}|$. The isotropic chemical shielding is an average over the principal components: $\sigma_{iso} = \frac{(\sigma_{xx} + \sigma_{yy} + \sigma_{zz})}{3}$ and the anisotropy is defined as $\sigma_{aniso} = \sigma_{zz} - \sigma_{iso}$. The asymmetry is obtained according to $\eta_{asym} = \frac{\sigma_{yy} - \sigma_{xx}}{\sigma_{ansio}}$, with $\eta_{asym} = 0$ corresponding to axial symmetry.

To compare the calculated chemicals shieldings to experimental chemical shift data, referencing according to the following scheme is required: $\delta_{iso} = \sigma_{ref} - \sigma_{iso}$.[23] For the discussed nuclei ^{1}H and ^{13}C, the references values and their origins are given below:

Table S5: *Summary of the nuclei, for which NMR parameters were calculated using the GIPAW (CASTEP) approach and the corresponding references values used to convert chemical shieldings into chemical shifts.*

nucleus	σ_{ref}	ref.
^{13}C	170.81 (**BINMEQ06** and **BINMEQ07**)	exact value by plotting exp. chem. shifts and calc. shieldings (fixed slope at −1)[23-24]

S7.2 Crystal vs. Molecule

To gain additional theoretical insight into the set of intermolecular interactions that are present for a particular form or packing arrangement, a second set of calculations was performed on a single molecule. To do so, one molecule from the fully geometry optimized structure was kept in the unit cell, which was also enlarged by ~5 Å in each direction. Thereby it was assured that this molecule is no longer in proximity to any neighbouring molecules. Subsequently, another set of NMR parameters was

calculated. Thus, the obtained chemical shifts were compared to the corresponding ones for the full crystal structure. This difference $\Delta\delta = \delta^{crystal} - \delta^{molecule}$ then represents the change induced by the sum of all interactions the molecule is involved in.

S7.3 GIPAW (CASTEP) calculations of Curcumin

Three different polymorphs, one monoclinic and two orthorhombic structures, of curcumin are known. The molecule exists in its keto-enol form. For the calculations in this project, we used the structures reported by Sanphui et al. in 2011.[18] They are deposited in the Cambridge Structural Database[25] under the following reference codes: CSD-BINMEQ05, CSD-BINMEQ06 and CSD-BINMEQ07 (**Figure S17**). Apart from the crystal system/space group and thus also the number of individual molecules in the asymmetric unit, the three structures also vary in the degree to which the two halves of the curcumin molecule are twisted (46° in BINMEQ05 vs. around 16° in BINMEQ06/07). The full table of crystal parameters can be found below (**Table S6**).

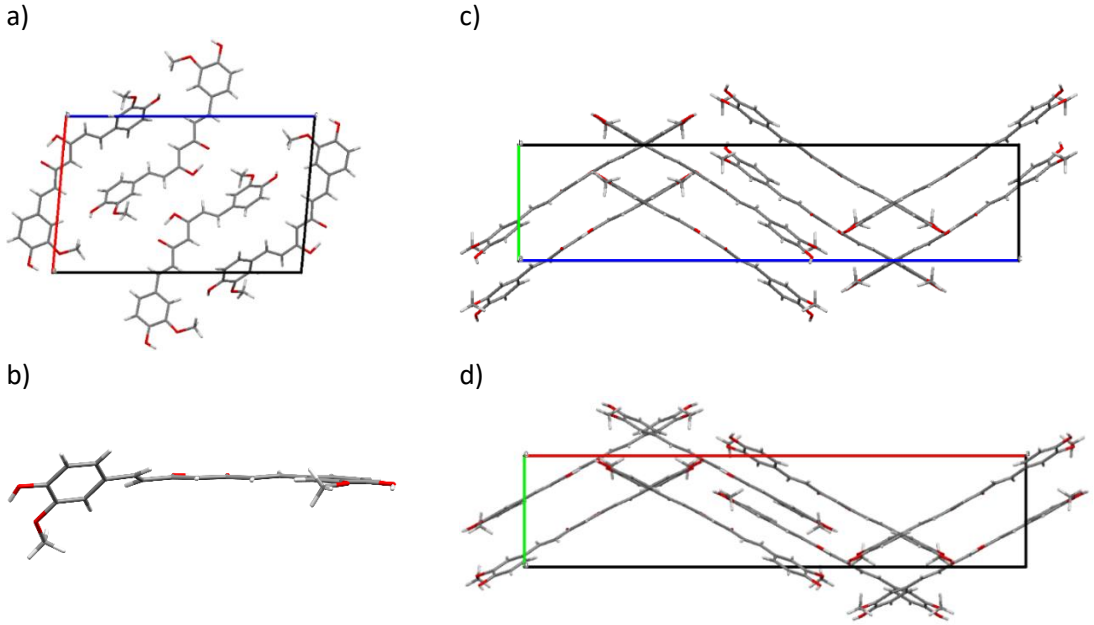

***Figure S17**: 1a,b) Representation of the full unit cell and the asymmetric unit for the monoclinic CUR crystal structure (BINMEQ05). On the right, the two monoclinic structures with the reference codes BINMEQ06 (1c) and BINMEQ (1d) are shown. For those two structures, the CUR molecules are almost flat, while the torsion angle in 1b) is 46°.*

***Table S6**: Summary of the characteristics of the three crystal forms of curcumin (BINMEQ05-07)[18] used for the calculations in this project. Interestingly, they differ in the degree to which the two halves of the CUR molecule are twisted.*

CCDC Code	**BINMEQ05**	**BINMEQ06**	**BINMEQ07**
Crystal System	monoclinic	orthorhombic	orthorhombic
Space Group	*P2/n*	*Pca2*$_1$	*Pbca*
$T_{measure}$ [K]	100	100	100
a [Å]	12.5676	35.417	12.536
b [Å]	7.0425	7.7792	7.9916
c [Å]	19.9582	12.6482	34.462
α [°]	90	90	90
β [°]	94.987	90	90
γ [°]	90	90	90
Z	4	8	8
Z'	1	2	1
Molecular Twist [°]	**46.0**	**18.6, 14.2**	**16.1**

The three crystal structures discussed above were used as starting point for the GIPAW (CASTEP) calculations. The resulting calculated stick spectra can be found in **Figure S18**. The calculated data for Form 1 and Form 2 agrees well with previous calculations made by other groups.[15, 26]

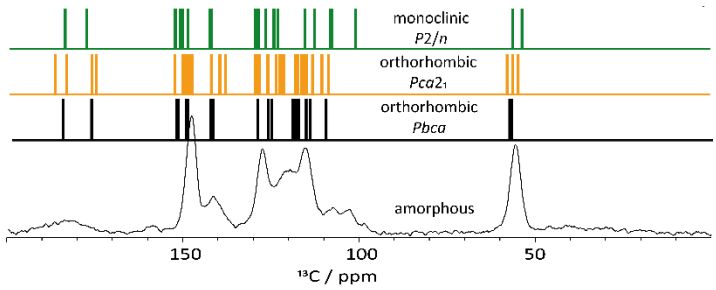

***Figure S18**: a) ^{13}C CP/MAS NMR spectra of quench-cooled amorphous CUR at 14.1 T and 24 kHz MAS alongside GIPAW (CASTEP) calculated chemical shifts.*

For the quench-cooled amorphous sample, the lines are considerably broadened. Interestingly, there is a broad feature at ~ 120 ppm, which is not observed in the initial untreated sample. The calculated data for two orthorhombic crystal structures predicts resonances in this spectral region. Both structures do not have the pronounced twist for the two halves of the molecule. Therefore, the amorphous sample should mostly contain curcumin molecules with a relatively flat, untwisted backbone. To learn more about key intermolecular interactions in the different polymorphs, which will help to understand the environment of CUR within the polymeric micelles, calculations for the crystal are compared to a single molecule calculated in an enlarged unit cell.

S7.4 GIPAW (CASTEP) calculations of Curcumin – crystal vs. molecule

After the initial full crystal geometry optimization, one molecule was selected and placed in an enlarged unit cell to calculate the chemical shifts in the absence of intermolecular interactions. The difference between this and the full crystal calculations are shown below (**Figure S19** and **Figure S20**). Generally, a positive difference for $\Delta\delta(^1H)$ is indicative of hydrogen bonding interactions, while a negative difference is observed if ring current effects are involved, e.g. for CH···π interactions.[27]

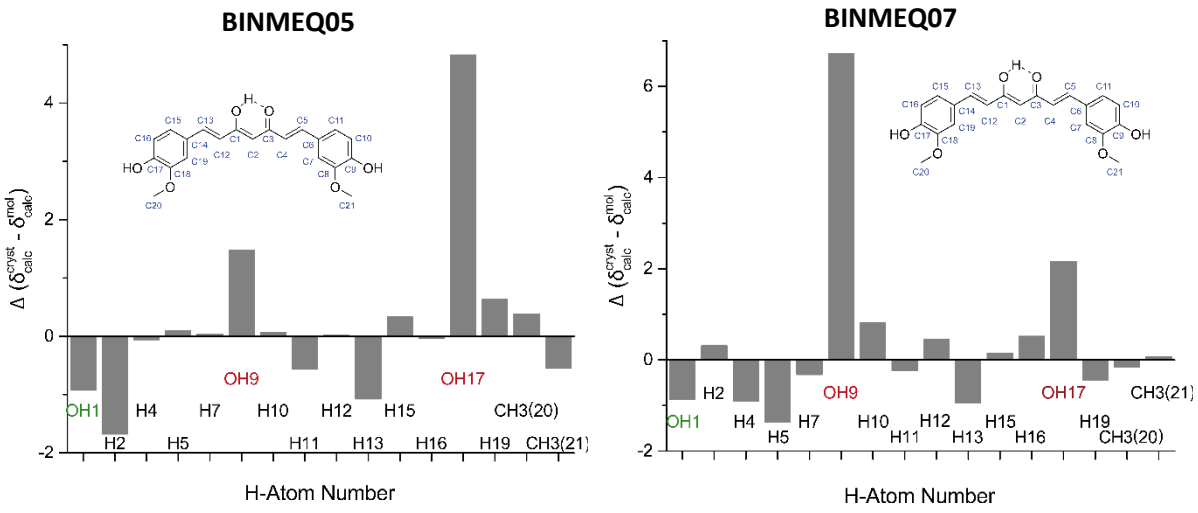

***Figure S19**: Crystal vs. molecule GIPAW NMR shielding calculation for the two polymorphs BINMEQ05 and BINMEQ07 each containing one molecule of CUR in the asymmetric unit. The differences plotted are obtained from one calculation for the full crystalline environment and one for a single molecule only.*

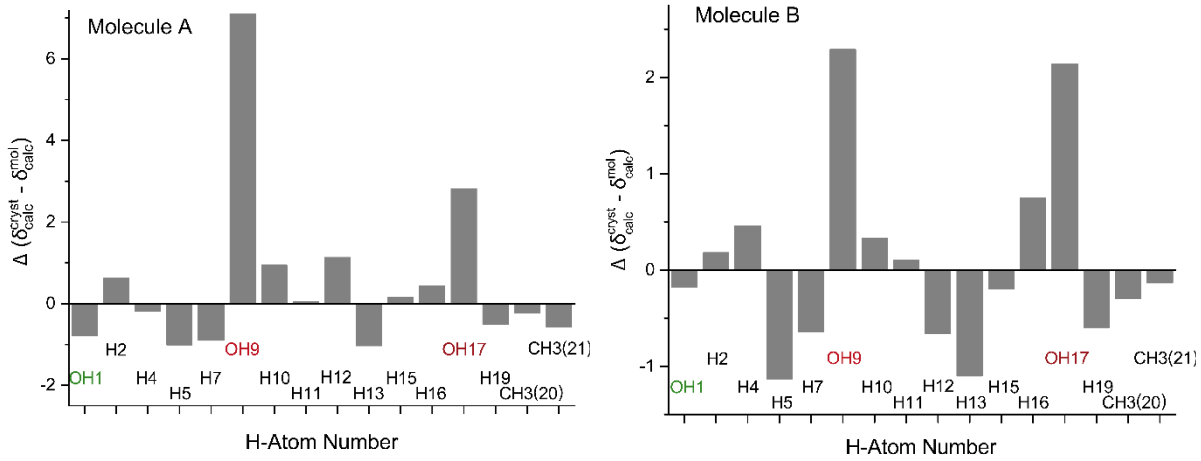

***Figure S20**: Crystal vs. molecule GIPAW NMR shielding calculation for the two individual molecules of CUR in the asymmetric unit of BINMEQ06. The differences plotted are obtained from one calculation for the full crystalline environment and one for each of the single molecule only.*

Throughout all the different graphs, the OH protons at each side of the curcumin molecule (highlighted in red) are most involved in hydrogen bonding as becomes apparent form the large positive difference between the crystal and the single molecule calculation. In contrast, all other interactions are less pronounced and also the other OH proton, which is part of the keto-enol group, is involved in strong intramolecular interactions but not in strong intermolecular interactions. Therefore, in the formulations, the CUR molecule is unlikely to interact with the polymer via this functional group.

S8. GIPAW(CASTEP) calculations of OH···O=CN interactions

To support the hypothesized structural model, additional GIPAW (CASTEP) calculations of three different crystal structure were performed. All structures contain at least on OH···O=CN interaction and the structures were selected so that they contain no additional functional groups and the effect of the interaction on the chemical shift is clearly distinguishable. The chemical formula and the CCDC code for the following three molecules are shown in **Figure S21**:

a) The isolated natural product 3-(2-Hydroxyphenyl)-1-(piperidin-1-yl) propan-1-one,[28]
b) the alkaloid Erythrinarbine (8-methoxy-9-hydroxy-1,2,5,6-tetrahydropyrrolo[2,1-a]isoquinolin-3(10bH)-one)[29]
c) and a cocrystal of hydroquinone with bis-(N,N-diethyl)bicyclo[2.2.2]octane-1,4-dicarboxamide.[30]

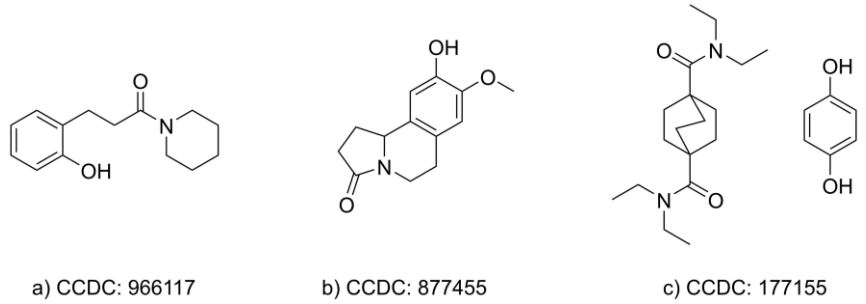

a) CCDC: 966117 b) CCDC: 877455 c) CCDC: 177155

Figure S 21*: Summary of the molecules used to obtain additional information on OH···O=CN interactions and the CCDC code of the respective crystal structures used for the GIPAW (CASTEP) calculations.*

For each of the structures, an NMR calculation of the full crystal was compared to the NMR calculation of a single, separated molecule as described in chapter S7.4. A set of relevant calculated changes in shown below:

Table S7: *Changes in chemical shifts between the full crystal structure and a separated molecule for selected functional groups in the molecules a)-c) presented above.*

Nucleus	**Moiety**	**Δδ(cryst.-mol.) in ppm**		
		a)	b)	c)
^{1}H	OH	6.5	6.6	5.4
	OMe	-	0.03	-
^{13}C	C-OH (hydroxy)	2.0	1.0	1.0
	C=O (amide)	2.0	4.0	2.0
	OMe	-	1.6	-
^{15}N	O=CN	13.1	13.8	16.9

These calculations can hint at the changes occurring for OH···O=CN interactions, in particular the strong increase in ^{1}H chemical shift for the OH group. For a more realistic representation also including the presence of more than one polymer chain and the geometrical arrangement of the polymers inside the micelle, more sophisticated modelling studies are necessary.

S9. References

[1] M. M. Lübtow, L. Hahn, M. S. Haider, R. Luxenhofer, *J. Am. Chem. Soc.* **2017**, *139*, 10980-10983.

[2] R. Luxenhofer, A. Schulz, C. Roques, S. Li, T. K. Bronich, E. V. Batrakova, R. Jordan, A. V. Kabanov, *Biomaterials* **2010**, *31*, 4972-4979.

[3] R. Wang, J. Han, A. Jiang, R. Huang, T. Fu, L. Wang, Q. Zheng, W. Li, J. Li, *Int. J. Pharm.* **2019**, *561*, 9-18.

[4] T. Gravestock, K. Box, J. Comer, E. Frake, S. Judge, R. Ruiz, *Analytical Methods* **2011**, *3*, 560-567.

[5] H. H. Tønnesen, J. Karlsen, *Zeitschrift für Lebensmittel-Untersuchung und Forschung* **1985**, *180*, 402-404.

[6] a) H. Hatcher, R. Planalp, J. Cho, F. M. Torti, S. V. Torti, *Cell. Mol. Life Sci.* **2008**, *65*, 1631-1652; b) J. Martínez-Guerra, M. Palomar-Pardavé, M. Romero-Romo, S. Corona-Avendaño, A. Rojas-Hernández, M. Ramírez-Silva, *Int. J. Electrochem. Sci* **2019**, *14*, 5373-5385.

[7] a) J. F. Young, *J. Appl. Chem.* **1967**, *17*, 241-245; b) L. Greenspan, *Journal of research of the national bureau of standards* **1977**, *81*, 89-96.

[8] F. Payton, P. Sandusky, W. L. Alworth, *J. Nat. Prod.* **2007**, *70*, 143-146.

[9] D. H. Wu, A. D. Chen, C. S. Johnson, *Journal of Magnetic Resonance, Series A* **1995**, *115*, 260-264.

[10] A. Jerschow, N. Müller, *J. Magn. Reson.* **1997**, *125*, 372-375.

[11] R. Evans, Z. Deng, A. K. Rogerson, A. S. McLachlan, J. J. Richards, M. Nilsson, G. A. Morris, *Angew. Chem. Int. Ed.* **2013**, *52*, 3199-3202.

[12] M. M. Lübtow, L. C. Nelke, J. Seifert, J. Kühnemundt, G. Sahay, G. Dandekar, S. L. Nietzer, R. Luxenhofer, *J. Control. Release* **2019**, *303*, 162-180.

[13] M. M. Lubtow, H. Marciniak, A. Schmiedel, M. Roos, C. Lambert, R. Luxenhofer, *Chemistry* **2019**, *0*.

[14] Q. Yu, D. Pichugin, M. Cruz, G. Guerin, I. Manners, M. A. Winnik, *Macromolecules* **2018**, *51*, 3279-3289.

[15] X. Kong, A. Brinkmann, V. Terskikh, R. E. Wasylishen, G. M. Bernard, Z. Duan, Q. Wu, G. Wu, *J. Phys. Chem. B* **2016**, *120*, 11692-11704.

[16] P. Duan, J. C. Moreton, S. R. Tavares, R. Semino, G. Maurin, S. M. Cohen, K. Schmidt-Rohr, *J. Am. Chem. Soc.* **2019**.

[17] S. Bates, G. Zografi, D. Engers, K. Morris, K. Crowley, A. Newman, *Pharm. Res.* **2006**, *23*, 2333-2349.

[18] P. Sanphui, N. R. Goud, U. B. R. Khandavilli, S. Bhanoth, A. Nangia, *Chem. Commun.* **2011**, *47*, 5013-5015.

[19] a) S. J. Clark, M. D. Segall, C. J. Pickard, P. J. Hasnip, M. I. J. Probert, K. Refson, M. C. Payne, *Z. Kristallogr.* **2005**, *220*, 567; b) C. J. Pickard, F. Mauri, *Phys. Rev. B* **2001**, *63*, 245101; c) J. R. Yates, C. J. Pickard, F. Mauri, *Phys. Rev. B* **2007**, *76*, 024401.

[20] J. P. Perdew, K. Burke, M. Ernzerhof, *Phys. Rev. Lett.* **1996**, *77*, 3865-3868.

[21] D. Vanderbilt, *Phys. Rev. B* **1990**, *41*, 7892-7895.

[22] S. Sturniolo, T. F. Green, R. M. Hanson, M. Zilka, K. Refson, P. Hodgkinson, S. P. Brown, J. R. Yates, *Solid State Nucl. Magn. Reson.* **2016**.

[23] R. K. Harris, P. Hodgkinson, C. J. Pickard, J. R. Yates, V. Zorin, *Magn. Res. Chem.* **2007**, *45*, S174-S186.

[24] G. N. M. Reddy, D. S. Cook, D. Iuga, R. I. Walton, A. Marsh, S. P. Brown, *Solid State Nucl. Magn. Reson.* **2015**, *65*, 41-48.

[25] C. R. Groom, I. J. Bruno, M. P. Lightfoot, S. C. Ward, *Acta Crystallogr. B* **2016**, *72*, 171-179.

[26] M. A. Matlinska, R. E. Wasylishen, G. M. Bernard, V. V. Terskikh, A. Brinkmann, V. K. Michaelis, *Cryst. Growth Des.* **2018**, *18*, 5556-5563.

[27] a) J. R. Yates, T. N. Pham, C. J. Pickard, F. Mauri, A. M. Amado, A. M. Gil, S. P. Brown, *J. Am. Chem. Soc.* **2005**, *127*, 10216-10220; b) A.-C. Uldry, J. M. Griffin, J. R. Yates, M. Pérez-Torralba, M. D. Santa María, A. L. Webber, M. L. L. Beaumont, A. Samoson, R. M. Claramunt, C. J. Pickard, S. P. Brown, *J. Am. Chem. Soc.* **2008**, *130*, 945-954.

[28] M. Parveen, A. M. Malla, M. Alam, F. Ahmad, P. S. P. Silva, M. R. Silva, *Natural Product Research* **2014**, *28*, 646-652.

[29] J. Selvakumar, R. S. Rao, V. Srinivasapriyan, S. Marutheeswaran, C. R. Ramanathan, *Eur. J. Org. Chem.* **2015**, *2015*, 2175-2188.

[30] B. M. Foxman, D. J. Guarrera, R. Pai, C. Tassa, J. C. Warner, *Cryst. Eng.* **1999**, *2*, 55-64.